Estimating Single-Epoch Integrated Atmospheric Refractivity from InSAR for Assimilation in Numerical Weather Models

Mulder, Gert; Van Leijen, Freek J.; Barkmeijer, Jan; De Haan, Siebren; Hanssen, Ramon F.

DOI
10.1109/TGRS.2022.3177041

Publication date
2022

Document Version
Final published version

Published in
IEEE Transactions on Geoscience and Remote Sensing

Citation (APA)
Mulder, G., Van Leijen, F. J., Barkmeijer, J., De Haan, S., & Hanssen, R. F. (2022). Estimating Single-Epoch Integrated Atmospheric Refractivity from InSAR for Assimilation in Numerical Weather Models. *IEEE Transactions on Geoscience and Remote Sensing*, *60*, Article 4108612. https://doi.org/10.1109/TGRS.2022.3177041

Estimating Single-Epoch Integrated Atmospheric Refractivity From InSAR for Assimilation in Numerical Weather Models

Gert Mulder, Freek J. van Leijen, *Member, IEEE*, Jan Barkmeijer, Siebren de Haan, and Ramon F. Hanssen, *Senior Member, IEEE*

***Abstract*— Numerical weather prediction (NWP) models are used to predict the weather based on current observations in combination with physical and mathematical models. Yet, they are limited by the spatial density and the accuracy of the available observations. Satellite radar interferometry (InSAR) is known to be extremely sensitive to the 3-D atmospheric refractivity distribution and has a high spatial resolution, providing information that can be used for assimilation in NWP models. However, due to the inherent superposition of two or more atmospheric states, only biased and temporally differenced signals can be retrieved, which can also be contaminated by deformation signals and decorrelation. Here, we present a method to estimate single-epoch absolute atmospheric delays by combining InSAR time series with prior NWP model prediction time series, using a constrained least-squares estimation. We show that this leads to a solution that reliably extracts the single-epoch relative delays from InSAR data and uses prior NWP model data to find the absolute reference for these delays while mitigating long-term deformation and decorrelation signal. This approach leads to repetitive delay updates with a spatial resolution of 500 m, which can be directly assimilated into numerical weather models.**

***Index Terms*— Atmospheric delay, InSAR, numerical weather prediction (NWP) model, single epoch.**

I. Introduction

OPERATIONAL numerical weather prediction (NWP) models have evolved over the years to deliver predictions with improving accuracy, reliability, and resolution [1]. However, high-resolution models also need reliable high-resolution inputs [2]. The integration of spaceborne InSAR measurements can significantly improve the quality of short-term predictions [3], [4]. While atmospheric measurements from InSAR have been a very promising data source to improve weather models for a long time [3], [5]–[7], they lacked the continuity and temporal sampling to have an impact in operational weather model predictions. This changed with the launch of the Sentinel-1 satellites in 2014 and 2016, providing a near-daily revisit potential over mid-latitudes [8], to be only further improved by current and planned X-, C-, or L-band missions.

Unfortunately, InSAR results are always relative—differenced in time and space—which causes a superposition of atmospheric states and introduces an unknown bias. Due to the time difference between subsequent acquisitions, the InSAR data may also be affected by nuisance signals such as surface deformation and decorrelation [9], while we assume that the topographic phase and the phase contribution due to the ionosphere are known or can be estimated independently [10].

To prevent most decorrelation and deformation issues, we can use single short-temporal baseline interferograms in combination with a weather model or GNSS result during one of the two acquisitions to estimate the atmospheric delay in the other acquisition [4], [11], [12]. However, this approach relies entirely on the external weather model or GNSS information to disentangle the mixed atmospheric states, instead of using the potential to do so from the InSAR data itself.

Here, we propose a new method, using a regularized least-squares solution combining the time series of InSAR observations and time series of previous NWP model predictions, to estimate the most recent single-epoch delay signal. The method deploys NWP time series, up to (i.e., not including) the time of the latest SAR acquisition. For operational NWP applications, this ensures that the results of the InSAR estimation update are independent of the current NWP realization. This allows us to disentangle the individual phase components, without using any additional assumptions. The model creates an absolute reference for the InSAR atmospheric delays using the NWP model data, with a minimal influence on the estimated variable delays. Finally, due to the addition of NWP data, we ensure a robust model solution, as it can provide an estimate even in the case of intermittent coherence loss and mitigate long-term deformations. Fig. 1 shows an overview of the proposed method. The resulting single-epoch delay product can directly be used by assimilation techniques such as 3-D variational (3-D-VAR) [13] and 4-D variational (4-D-VAR) [14], such as in [15], and explicit translation of delay values in precipitable water vapor (PWV) [12], [16], [17], which is therefore not needed.

Manuscript received November 9, 2021; revised March 18, 2022; accepted April 8, 2022. Date of publication May 23, 2022; date of current version June 22, 2022. This work was supported by the Dutch Research Council (NWO) under Project ALW-GO/14-39. *(Corresponding author: Gert Mulder.)*

Gert Mulder is with the Department of Geoscience and Remote Sensing, Delft University of Technology, 2600 AA Delft, The Netherlands, and also with the Royal Netherlands Meteorological Institute (KNMI), 3730 AE De Bilt, The Netherlands (e-mail: g.mulder-1@tudelft.nl).

Freek J. van Leijen and Ramon F. Hanssen are with the Department of Geoscience and Remote Sensing, Delft University of Technology, 2600 AA Delft, The Netherlands (e-mail: f.j.vanleijen@tudelft.nl; r.f.hanssen@tudelft.nl).

Jan Barkmeijer and Siebren de Haan are with the Royal Netherlands Meteorological Institute (KNMI), 3730 AE De Bilt, The Netherlands.

Digital Object Identifier 10.1109/TGRS.2022.3177041

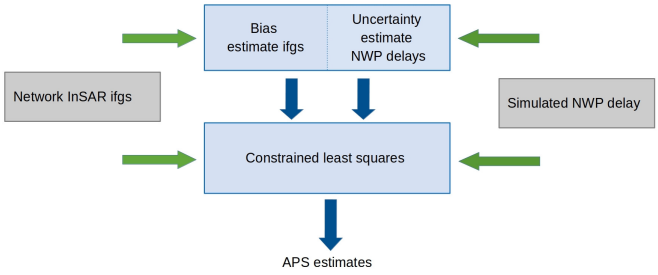

Fig. 1. Main steps to estimate absolute single-epoch delays. The inputs of the procedure are: 1) a set of interferometric combinations and associated coherences and 2) a stack of atmospheric delays based on NWP model realizations. Before the constrained least-squares estimation, the single biases per interferogram and the NWP model uncertainty are estimated. Both estimation methods use a combination of unwrapped interferograms and NWP model delays. After the biases and NWP model uncertainty are obtained, the absolute single-epoch delays can be estimated using the bias-corrected InSAR interferograms, the predicted NWP data, and the uncertainty estimations of both datasets.

In Section II, we describe how we derive absolute single-epoch delays using a time series of InSAR delays and former numerical weather model states, followed by a demonstration of the method in Section III. In Section IV, we draw general conclusions on its merits and applicability.

II. Methods

To isolate the delay values of individual (single-epoch) acquisitions from the differential InSAR data, three challenges should be tackled. First, as the observed differential atmospheric delay $\delta_p^{t_i,t_j}$ at position p in an interferogram spanning, (t_i, t_j) is the difference between two unknown single atmospheric delays, $\delta_p^{t_i}$ and $\delta_p^{t_j}$, and the superposed atmospheric signals should be disentangled. Second, the subtraction of the two atmospheric states eliminates the common mode, $\delta_{\mathrm{cm},p}$, i.e., the spatially variable but time-invariant part of the delay signal. The common mode is often related to the topography of the area as the total delay declines with elevation [18]. Third, due to the double-differenced and wrapped nature of the interferometric phase, all SAR acquisitions have an unknown bias, $\delta_{\mathrm{bias}}^{t_i}$, which is the delay of the selected reference point q, which is constant for the entire scene. Hence, the single-epoch atmospheric delay signal $\delta_p^{t_i}$ that we wish to retrieve is

$$\delta_p^{t_i} = \delta_{\mathrm{var},p,q}^{t_i} + \delta_{\mathrm{cm},p} + \delta_{\mathrm{bias}}^{t_i} \tag{1}$$

where $\delta_{\mathrm{var},p,q}^{t_i} = \delta_{\mathrm{var},p}^{t_i} - \delta_{\mathrm{bias}}^{t_i}$ is the spatially variable part of the delay signal, which is zero at the reference point q. Consequently, the atmospheric contribution in an interferogram between t_i and t_j at position p is

$$\begin{aligned}\delta_p^{t_i,t_j} &= \delta_p^{t_i} - \delta_p^{t_j},\\ &= \delta_{\mathrm{var},p,q}^{t_i} - \delta_{\mathrm{var},p,q}^{t_j} + \delta_{\mathrm{bias}}^{t_i} - \delta_{\mathrm{bias}}^{t_j}\\ &= \delta_{\mathrm{var},p,q}^{t_i} - \delta_{\mathrm{var},p,q}^{t_j} + \delta_{\mathrm{bias}}^{t_i,t_j}.\end{aligned} \tag{2}$$

Since the interferogram is a double-difference phase between two points

$$\phi_{p,q}^{t_i,t_j} = \phi_p^{t_i,t_j} - \phi_q^{t_i,t_j} \tag{3}$$

with $\phi_p^{t_i,t_j} = (4\pi/\lambda)\delta_p^{t_i,t_j}$, the expectation of the interferometric phase then relates to the delay signals as

$$\begin{aligned}E\left\{\phi_{p,q}^{t_i,t_j}\right\} &= \frac{4\pi}{\lambda}\left(\delta_p^{t_i,t_j} - \delta_{\mathrm{bias}}^{t_i,t_j}\right)\\ &= \frac{4\pi}{\lambda}\left(\delta_{\mathrm{var},p,q}^{t_i} - \delta_{\mathrm{var},p,q}^{t_j}\right)\end{aligned} \tag{4}$$

where $\phi_p^{t_i,t_j}$ is the observed unwrapped atmospheric phase and the bias $\delta_{\mathrm{bias}}^{t_i,t_j}$ is the differential delay value at reference point q.

Since we wish to retrieve $\delta_p^{t_i}$ and $\delta_p^{t_j}$ from (1) and the InSAR data is only sensitive to $\delta_{\mathrm{var},p,q}^{t_i}$ and $\delta_{\mathrm{var},p,q}^{t_j}$, as shown in (4), it is not possible to derive $\delta_{\mathrm{cm,p}}$ and $\delta_{\mathrm{bias}}^{t_i,t_j}$ without external information. Yet, it is possible to estimate $\delta_{\mathrm{var},p,q}^{t_i}$ in (4) for every acquisition using combinations of interferograms. For example, Liu [19] and Leijen and Hanssen [20] estimated the single-epoch atmospheric phase screen (APS) using techniques such as small-baseline subset (SBAS) [21] or phase linking [22] on a series of interferograms, while Hooper *et al.* [23], Ferretti *et al.* [24], [25], and Leijen [26] developed techniques to find the APS based on PSI techniques. However, these solutions do not consider the time-invariant part of the delay signal, $\delta_{\mathrm{cm},p}$. An alternative to estimate $\delta_{\mathrm{bias}}^{t_i}$ is by using additional data sources, such as GNSS-derived tropospheric delays [27], [28] or MERIS water vapor estimates [29], [30], but GNSS data have a much lower spatial coverage than InSAR and MERIS could only be used under cloudless conditions for the ENVISAT satellite mission.

Assuming that the influence of topography and ionospheric signal can be mitigated effectively using a digital elevation model and an ionospheric model, respectively (see [18], [31]), the influence of decorrelation noise and surface deformation needs to be accounted for.

Decorrelation noise can often be mitigated by spatial filtering or by using alternative interferometric combinations [22]. Disturbances due to deformations are more difficult to detect. In this study, we assume that strong deformations due to earthquakes, landslides, or volcanic activity did not occur during the study period, but other small deformation signals may still contaminate the results.

Although such deformations may typically be small compared to the total atmospheric signal in two subsequent SAR acquisitions, they can accumulate over longer time spans when using methods such as SBASs [21] or phase linking [22].

A. Setup Constrained Least Squares

To estimate the APS in the most recent radar acquisition, a constrained least-squares estimation is used [32], on a time series of n SAR acquisitions [see Fig. 2(a)] and their corresponding NWP model realizations, up to acquisition $n-1$. The InSAR data contain unwrapped interferograms in a "network approach," i.e., limited to the interferometric combinations within a maximum time window of $\Delta t_{\max} = 60$ days (see Fig. 2), yielding a subset of n SAR acquisitions.

This network approach is required to mitigate the influence of reversible short-term decorrelation, such as snow, on the delay estimate in the short term and irreversible temporal decorrelation in the long term. Figs. 2(a)–(c) shows that to

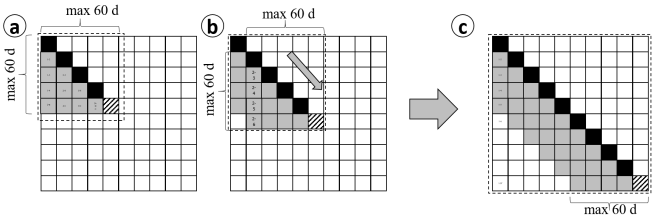

Fig. 2. Computational approach for n SAR acquisitions, where n is increasing in time. (a) Lower triangular matrix showing all possible interferometric combinations in gray, the NWP model realizations in black, and the new atmospheric delay estimate hatched. (b) For growing time series, a maximum temporal baseline of 60 days is used, leading to (c) bandwidth of interferometric combinations.

subsequently estimate the APS of the most recent acquisition, we apply a band-limited set of acquisitions.

From the NWP model, a time series of single-epoch atmospheric delays $\delta^{t_i}_{\mathrm{NWP},p}$ is computed by integration of the refractivity over the slant signal path [33], [34], see Section II-C. This serves as an absolute reference and a filter for long-term deformations (see Fig. 1) and the black boxes in Fig. 2. In this way, we use both the higher accuracy of the InSAR measurements for single epoch and the reliability of the long-term average of the NWP model. The network for the constrained least-squares estimation is now modeled as

$$E\{\underline{y}\} = Ax;\ D\{\underline{y}\} = Q_y \tag{5}$$

where x is the $n \times 1$ vector with the absolute APS for individual epochs $\delta^{t_i}_p$, of which the last epoch, n, has our main interest. The expectation and dispersion operators are indicated by $E\{\}$ and $D\{\}$, respectively. The underlined stochastic observation vector $\underline{y}$ is a combination of the phase values of the network of interferograms and predicted NWP model phases

$$\underline{y} = \begin{bmatrix} \frac{\lambda}{4\pi}\underline{\phi}^{t_1,t_2}_{p,q} - \underline{\delta}^{t_1,t_2}_{\mathrm{bias}} \\ \frac{\lambda}{4\pi}\underline{\phi}^{t_1,t_3}_{p,q} - \underline{\delta}^{t_2,t_3}_{\mathrm{bias}} \\ \vdots \\ \frac{\lambda}{4\pi}\underline{\phi}^{t_{n-1},t_n}_{p,q} - \underline{\delta}^{t_{n-1},t_n}_{\mathrm{bias}} \\ \underline{\delta}^{t_1}_{\mathrm{NWP},p} \\ \underline{\delta}^{t_2}_{\mathrm{NWP},p} \\ \vdots \\ \underline{\delta}^{t_{n-1}}_{\mathrm{NWP},p} \end{bmatrix} \tag{6}$$

where $\underline{\phi}^{t_i,t_j}_{p,q}$ is the unwrapped InSAR phase of a specific pixel $p = \{1,\ldots,P\}$ from the interferogram with master image $i = \{1,\ldots,n-1\}$ and slave image $j = \{2,\ldots,n\}$ (see Section II-C). The total length of vector $\underline{y}$ is the total number of interferograms plus the total number of epochs. The estimated interferogram bias value, $\underline{\hat{\delta}}^{t_i,t_j}_{\mathrm{bias}}$, is constant for the entire interferogram and will be discussed in Section II-D. $\underline{\delta}^{t_i}_{\mathrm{NWP},p}$ is the predicted single-epoch phase from the weather model at time i for pixel p. The acquisition times start at t_1 and run until t_n, while for the NWP model data, the most recent acquisition, t_n, is not used, as we base our solution on historical NWP time series only. Matrix A relates the observations and single-epoch absolute delays and can be written as

$$A = \begin{bmatrix} A_\phi \\ A_\delta \end{bmatrix} \tag{7}$$

where the $p \times n$ design matrix $A_\phi = [A^T_{n-1}\cdots A^T_1]^T$, with elements $A_i = [O_{i,n-1-i}\,|\,J_{i,1}\,|\,-I_i]$ of the size $i \times n$. Here, $O_{i,j}$ is the $i \times j$ zero matrix, $J_{i,1}$ is the $i \times 1$ ones vector, I_i is the $i \times i$ identity matrix, and $p = n(n-1)/2$ and $A_\delta = [I_{n-1}\,|\,O_{n-1,1}]$. Thus, every line in A_ϕ represents one of the interferometric combinations given in Fig. 2 and every line in A_δ represents a predicted delay derived from the NWP, with the exception of the last epoch.

The system described in (5) is in our case a redundant system of equations, for which we can derive the best linear unbiased estimate (BLUE) [32], representing the absolute single-epoch atmospheric delays $\underline{\hat{x}}$

$$\underline{\hat{x}} = \left[\hat{\delta}^{t_1}_p, \hat{\delta}^{t_2}_p, \cdots \hat{\delta}^{t_n}_p\right]^T. \tag{8}$$

The cost function is defined as follows:

$$\min\left(\left\|\left(\hat{\delta}^{t_i}_p - \hat{\delta}^{t_j}_p - \hat{\delta}^{t_i,t_j}_{\mathrm{bias}}\right) - \frac{\lambda}{4\pi}\phi^{t_i,t_j}_{p,q}\right\|_{Q_\phi} + \left\|\hat{\delta}^{t_i}_p - \delta^{t_i}_{\mathrm{NWP},p}\right\|_{Q_\delta}\right) \tag{9}$$

where $\hat{\delta}^{t_i}$ is the previously estimated single-epoch absolute delay, $\hat{\delta}^{t_i,t_j}_{\mathrm{bias}}$ is the estimated image-wide bias, $\phi^{t_i,t_j}_{p,q}$ is the unwrapped interferometric phase, and $\delta^{t_i}_{\mathrm{NWP},p}$ is the calculated delay from the weather model. The covariance matrix of the InSAR data is Q_ϕ, see Section II-C, and the covariance matrix of the NWP model realizations is Q_δ, see Section II-F.

B. Interferometric Combinations

We use a maximum time window of $\Delta t_{\max} = 60$ days for the interferometric combinations. All the interferograms are coregistered and resampled based on the Sentinel-1 precise orbits, corrected for the topographic phase based on the STRM DEM, and georeferenced. In geographic coordinates, we define square grid cells of 500 m, for which the complex average is computed, and subsequently, this set is unwrapped using Snaphu [35]. If ionospheric trends are detected based on burst or swath discontinuities, they are removed from the stack.

C. Calculation APS From NWP Model

The predicted delays $\delta^{t_i}_{\mathrm{NWP}}$ from the NWP model are calculated by integrating the refractivity N along the radar signal path [34]. To compute the refractivity along the path, we apply [36]

$$N = k_1\frac{P_d}{T} + k_2\frac{e}{T} + k_3\frac{e}{T^2} + k_4\frac{n_e}{f^2} + k_5 W \tag{10}$$

where T is temperature in kelvin, e is the partial pressure of water vapor, P_d is the partial pressure of dry air, L is the liquid water content, n_e is the electron density per cubic meter, f is the radar frequency, and W is the liquid water content. The values of the constants are $k_1 = 77.6$, $k_2 = 71.6$, $k_3 = 3.75 \times 10^5$ [37], [38], $k_4 = -4.028 \times 10^7$ m^{-3}, and

$k_5 = 1.4\ \mathrm{m^3 g^{-1}}$. The last two terms represent the ionospheric refractivity and the refractivity due to liquid water in the atmosphere. However, the ionospheric term can be estimated independently of models [39], GNSS networks, or the SAR data [10] and the liquid water has a nonsignificant influence on the final solution [18], [31]. The total delay is calculated by integrating the refractivity over the slant signal path through the atmosphere. By ray tracing the slant InSAR radar path using the topographic heights from the SRTM DEM, we can account for the topographic effect in the weather model and create a smooth transition from the lower resolution NWP model to the 500-m geographical grid used for InSAR processing.

D. Bias Correction InSAR Differential APS

Assuming that the deformation in interferograms with $\Delta t_{\max} = 60$ days is negligible, we can obtain the absolute differential atmospheric delay, $\hat{\delta}^{t_i,t_j}_{\mathrm{ifg},p}$, by subtracting an unknown constant delay bias from the unwrapped observations

$$\hat{\delta}^{t_i,t_j}_{\mathrm{ifg},p} = \frac{\lambda}{4\pi}\phi^{t_i,t_j}_{p,q} - \hat{\delta}^{t_i,t_j}_{\mathrm{bias}}. \tag{11}$$

In conventional InSAR processing where the aim is to estimate deformation, the bias is introduced via a reference point or reference region, where deformation is assumed to be zero. However, this approach still disregards the atmospheric offset, which is of vital importance for our application. We estimate the bias $\hat{\delta}^{t_i,t_j}_{\mathrm{bias}}$ using the image-wide difference between the unwrapped interferogram and a synthetic interferogram based on two single-epoch NWP model delay estimates for grid cell p

$$\Delta\delta^{t_i,t_j}_{p} = \frac{\lambda}{4\pi}\phi^{t_i,t_j}_{p,q} - \left(\delta^{t_i}_{\mathrm{NWP},p} - \delta^{t_j}_{\mathrm{NWP},p}\right) \tag{12}$$

where $\delta^{t_i}_{\mathrm{NWP}}$ is the delay for scene i derived from NWP data at time t_i and ϕ^{t_i,t_j} is the interferogram between time i and j (see Fig. 3 for a visualization of this procedure). To estimate the bias from the differential interferogram $\Delta\delta^{t_i,t_j}_{p}$, averaging would be the easiest approach, but due to strong anomalies in either the model or InSAR data, this method is unreliable. For example, strong atmospheric disturbances due to thunderstorms have a strong influence on the final mean, while the size and locations of these disturbances generally differ significantly between the NWP model and InSAR data and should be disregarded. Therefore, we use the mode of the distribution $f_{\Delta\delta}$ of differences as an estimate of the bias (see Fig. 3)

$$\hat{\delta}^{t_i,t_j}_{\mathrm{bias}} = \arg\max_{\Delta\delta} f_{\Delta\delta}\left(\Delta\delta^{t_i,t_j}\right). \tag{13}$$

The estimated offsets for the different interferometric combinations are adjusted using a nonweighted least-squares solution to ensure that for every triplet of interferometric combinations, it holds

$$\hat{\delta}^{t_i,t_k}_{\mathrm{bias}} + \hat{\delta}^{t_k,t_j}_{\mathrm{bias}} + \hat{\delta}^{t_j,t_i}_{\mathrm{bias}} = 0. \tag{14}$$

This solution is then fed into the constrained least squares as given in (5). Here, the found biases are used as part of the observation matrix $\underline{y}$, assuming that they have minimal impact on the InSAR accuracies. Ideally, the biases would be included as unknowns in (5). However, this is not possible because the bias estimation is performed for the full interferogram, while the single-epoch absolute delay estimations are performed on a pixel-by-pixel basis.

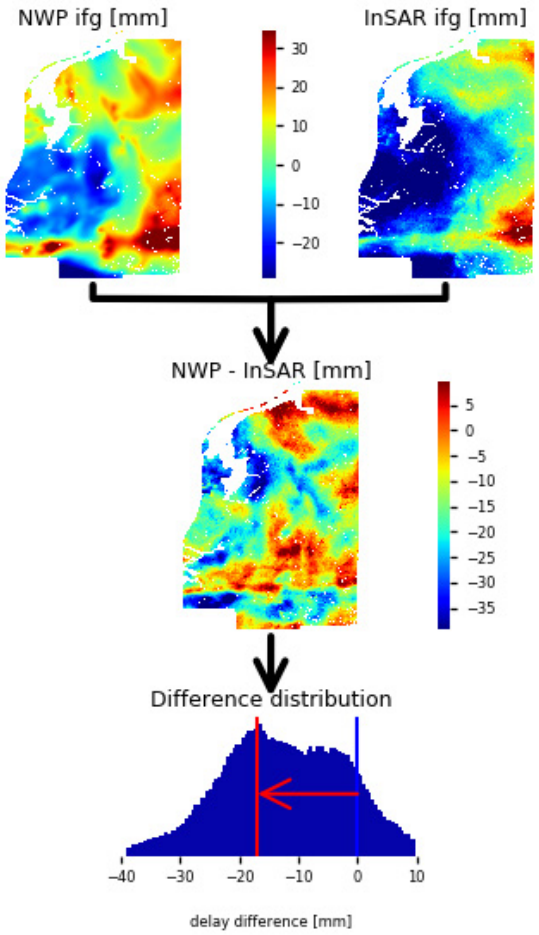

Fig. 3. Estimating bias per interferogram. The difference between the InSAR interferograms and the differenced NWP model delays is derived. The distribution of the resulting difference map is used to estimate the offset, from the mode of this distribution. This is equivalent to the largest area with similar patterns in the differential NWP model delays and InSAR interferogram.

E. Error Estimate InSAR Data

To estimate the precision of the InSAR data, i.e., Q_ϕ in (9), we estimate the coherence using a window of 500 × 500 m under the assumption of ergodicity [40], to derive the phase precision [18]. The equivalent multilooking window of 500 × 500 m may still result in temporal measurement gaps due to low coherence, e.g., due to snow. However, due to the inclusion of NWP model predictions, we can still connect the periods before and after these gaps and retrieve reliable estimates for all nonaffected interferograms.

F. Error Estimate Weather Model Data

A reliable estimate of the uncertainty in the NWP model delays, via covariance matrix Q_δ, is crucial for a correct

weighting of the NWP model data in our constrained least-squares solution. Therefore, we estimate these uncertainties based on a combination of InSAR interferograms and differential NWP model delays. To estimate Q_δ, we can use the *a priori* knowledge that the precision of the delay measurements from InSAR is much higher than that of the NWP model delays. If we can assume that the InSAR errors are negligible, the error of differential NWP model delays can be derived by subtracting the differential NWP delays from the InSAR data. Therefore,

$$e^{t_i,t_j}_{\mathrm{NWP},p} \approx e^{t_i,t_j}_{\mathrm{NWP,ifg},p} = \hat{\delta}^{t_i,t_j}_{\mathrm{ifg},p} - \left(\delta^{t_i}_{\mathrm{NWP},p} - \delta^{t_j}_{\mathrm{NWP},p}\right) \quad (15)$$

given that

$$e^{t_i,t_j}_{\mathrm{ifg},p} \ll e^{t_i,t_j}_{\mathrm{NWP},p}. \quad (16)$$

Here, e_{NWP} is the error in the synthetic NWP model interferograms, e_{ifg} the error in the InSAR interferograms, $\hat{\delta}^{t_i,t_j}_{\mathrm{ifg},p}$ is the bias corrected InSAR interferogram, and $\delta^{t_i}_{\mathrm{NWP},p}$ is the NWP model delay value for individual scenes. The retrieved NWP model error from (15) is used to estimate the local variance by squaring and applying a spatial averaging kernel

$$\sigma^2_{\delta,t_i,t_j,p} = G\left(e^{t_i,t_j}_{\mathrm{NWP},p}\right) \quad (17)$$

where $\sigma^2_{\delta,t_i,t_j,p}$ is the variance of the differential NWP model delays for a specific pixel and $G(x, y)$ is a Gaussian averaging kernel of 10 km, which is the effective resolution of the NWP model. This variance can be described as the sum of the variances of the two NWP scenes

$$\sigma^2_{\delta,t_i,t_j} = \sigma^2_{\delta,t_i} + \sigma^2_{\delta,t_j} \quad (18)$$

where $\sigma^2_{\delta,t_i,t_j}$ is the variance of the differential NWP model delays and σ^2_{δ,t_i} is the variance of an individual NWP model scene. An illustration of the full method is given in Fig. 4. From these added variances, we then estimate the variances of the individual scenes using a set of equations modeled as

$$E\{\underline{y}\} = A_\phi x \quad (19)$$

where y is the vector with the derived variances $\sigma^2_{\delta,i,j}$ for all the interferograms, x is the vector with the variances for the individual scenes $\sigma^2_{\delta,i}$, and matrix A_ϕ is the system of equations that relates the used interferometric combinations with the single-epoch values, as given in (7), but here with only positive values representing an addition in contrast with the subtraction for the intereformetric phase. The observation vector $\underline{y}$ is given by

$$\underline{y} = \begin{bmatrix} \sigma^2_{\delta,t_1,t_2} \\ \sigma^2_{\delta,t_2,t_3} \\ \vdots \\ \sigma^2_{\delta,t_{n-1},t_n} \end{bmatrix} \quad (20)$$

where $\sigma^2_{\delta,i,j}$ are the estimated variances for the differential NWP model delays. The total length of vector $\underline{y}$ is the total number of interferograms. The used cost function is

$$\min\left(\|\hat{\sigma}^2_{\delta,t_i,t_j} - \sigma^2_{\delta,t_i,t_j}\|\right) \quad (21)$$

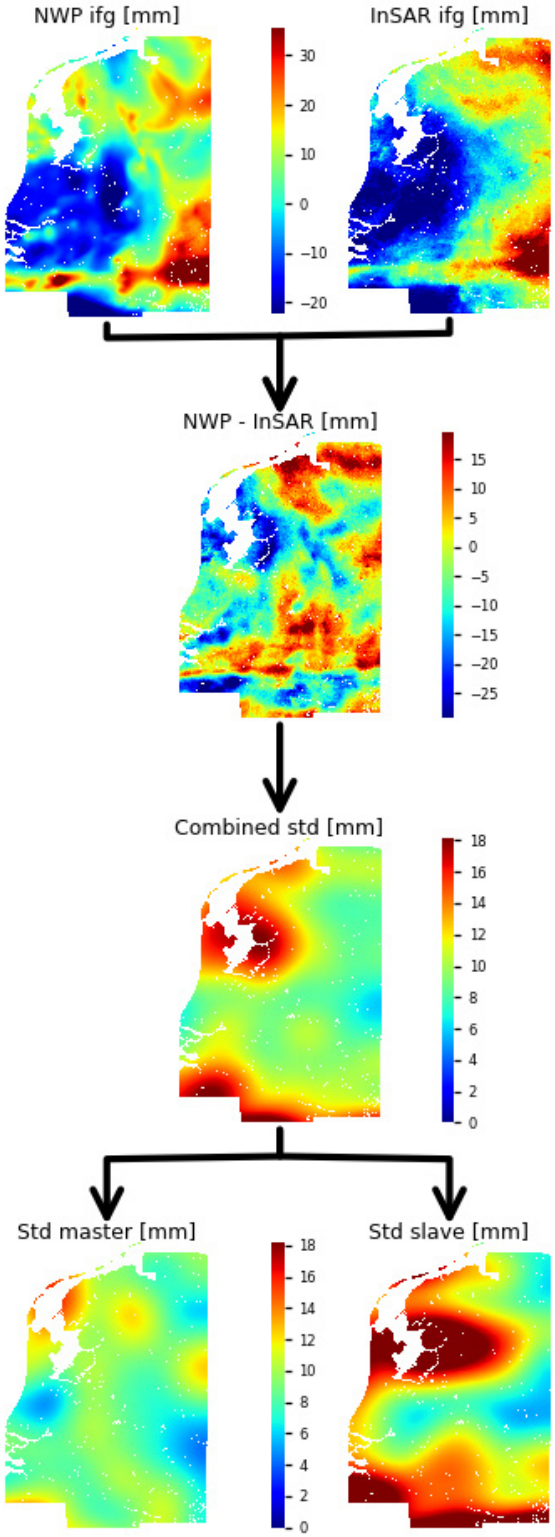

Fig. 4. Estimating the error in the NWP model. The difference between the InSAR interferogram and the differenced NWP model delays is squared and smoothed in space to get an approximation of the variance of the differenced NWP model delays. Subsequently, the variance of single NWP model delays is estimated using a least-squares solution.

where $\sigma^2_{\delta,i,j}$ are the variances of the differential NWP model delays and $\hat{\sigma}^2_{\delta,i,j}$ are the estimated variances based on the

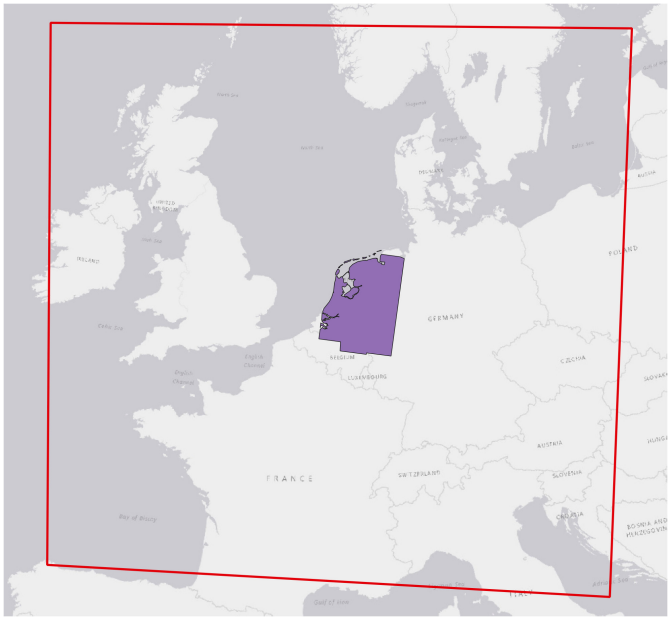

Fig. 5. Coverage of Harmonie model (red box) and Sentinel-1 track 37 (purple) over The Netherlands. Water areas are masked out.

solution for the individual scenes $\hat{x}$. After solving for x, this gives us the estimated NWP model delay variances $\hat{\sigma}^2_{\delta,t_i}$, which form the diagonal elements in the covariance matrix

$$Q_{\hat{\delta}} = \begin{bmatrix} \hat{\sigma}^2_{\delta,t_1} & 0 & \cdots & 0 \\ 0 & \hat{\sigma}^2_{\delta,t_2} & \cdots & 0 \\ \vdots & \vdots & \ddots & \vdots \\ 0 & 0 & \cdots & \hat{\sigma}^2_{\delta,t_n} \end{bmatrix}. \tag{22}$$

This approach may sometimes result in near-zero or even slightly negative variance estimates, but because our main focus is the scenes with large errors, we can safely apply a minimum error of a few millimeters for these scenes.

III. Results and Discussion

A. Model Inputs and Study Area

Time series of Sentinel-1 track 37 SAR data and NWP model data over The Netherlands between 2016 and 2018 are used (see Fig. 5). The SAR time series includes more than 120 VV-polarized SLC images with an original resolution of approximately 3 m $\times$ 20 m and yields a stack of geocoded C-band interferograms with a 500-m resolution after processing as described in II-B. We use the Harmonie NWP model—the operational model for The Netherlands—which is based on AROME [41]. The horizontal resolution is about 2.5 km and it consists of 65 vertical model levels. The spatial coverage of the model realizations for this study is about 2000×2000 km^2 centered at The Netherlands and nested within the operational European Centre for Medium-Range Weather Forecasts (ECWMF) global model [42].

B. Estimated Single-Epoch Atmospheric Delay Time Series

Fig. 6 presents five representative single-epoch atmospheric delay estimates, showing the NWP-derived delays, the estimated atmospheric delays, and the difference between both in the first, second, and third columns. The fourth column shows the distribution of the latter. Because the absolute slant delay images would be dominated by range effects—with a longer propagation path for far range pixels—for visualization, the slant delays, $\hat{\delta}^{t_i}_p$, are mapped to the zenith $\hat{\delta}^{t_1}_{\text{zenith},p}$ based on the incidence angle θ_p per pixel, using the mapping function $\hat{\delta}^{t_i}_{\text{zenith},p} = \hat{\delta}^{t_i}_p \cos\theta_p$.

Likewise, topographic elevation causes a significant shortening of the total propagation path, an effect that is automatically differenced out in interferograms. This is a dominant effect in a linear scaling factor, κ, and implements an artificial correction for the topography, with

$$\hat{\delta}^{t_i}_{\text{zenith},h,p} = \kappa\, h_p + \hat{\delta}^{t_i}_{\text{zenith},p} \tag{23}$$

where $\hat{\delta}^{t_i}_{\text{zenith},h,p}$ is the delay corrected for the topography, h_p is the height per pixel, and κ is the fit scaling factor of $\sim$1 mm/m. Fig. 7 shows the changes of single-epoch zenith delays due to this topographical correction. This linear model is only valid from sea level until 300 m height, which is the height range over The Netherlands. For larger height differences, an exponential model will be needed, as the refractivity N varies exponentially over height.

Evaluating 120 topography-adjusted single-epoch zenith delays as a function of time shows a clear seasonal variability, see Fig. 8, with greater delays in summer, when the warmer air can contain more water vapor, compared with winter. The variability of the delays over the scene is also greater in summer, as indicated by the ranges in the boxplots. Similar trends can be observed in the differences between the estimated single-epoch delays and the predicted NWP model delays (see Fig. 9). The average values are close to zero, as expected, but the range of variation within the image is larger during the summer period. Especially with strong convective events like thunderstorms these differences are large.

C. Residuals of Estimated Delay and InSAR or NWP Model

To verify whether the results of the original unwrapped interferograms are sustained in the final delay estimate, we compare the residuals of the InSAR interferograms for subsequent dates with the difference of the single-epoch delay estimates, which corresponds to the first part of the cost function of (9), i.e.,

$$\sigma^2_{\text{ifg}}(t_i) = \frac{1}{P}\sum_{p=1}^{P} \left|\left|\left(\hat{\delta}^{t_i}_p - \hat{\delta}^{t_j}_p - \hat{\delta}^{t_i,t_j}_{\text{bias}}\right) - \frac{\lambda}{4\pi}\phi^{t_i,t_j}_{p,q}\right|\right| \tag{24}$$

where $\sigma^2_{\text{ifg}}(t_i)$ is the standard deviation per interferogram and P is the number of pixels in the image. The daisy-chain choice for this evaluation mitigates the influence of potential deformation and decorrelation. Fig. 10 shows these average absolute residuals per interferogram, indicated in blue, which are in the order of few millimeters at most. Similarly, a comparison can be made between the NWP realizations and single-epoch estimates, which corresponds with the second part of the cost function in (9). To compare these values with the InSAR residuals, we combine the residuals for both time steps of the interferogram as

$$\sigma^2_{\text{NWP}}(t_i) = \frac{1}{P}\sum_{p=1}^{P} \left|\left|\left(\hat{\delta}^{t_i}_p - \delta^{t_i}_{\text{NWP},p}\right) - \left(\hat{\delta}^{t_{i+1}}_p - \delta^{t_{i+1}}_{\text{NWP},p}\right)\right|\right| \tag{25}$$

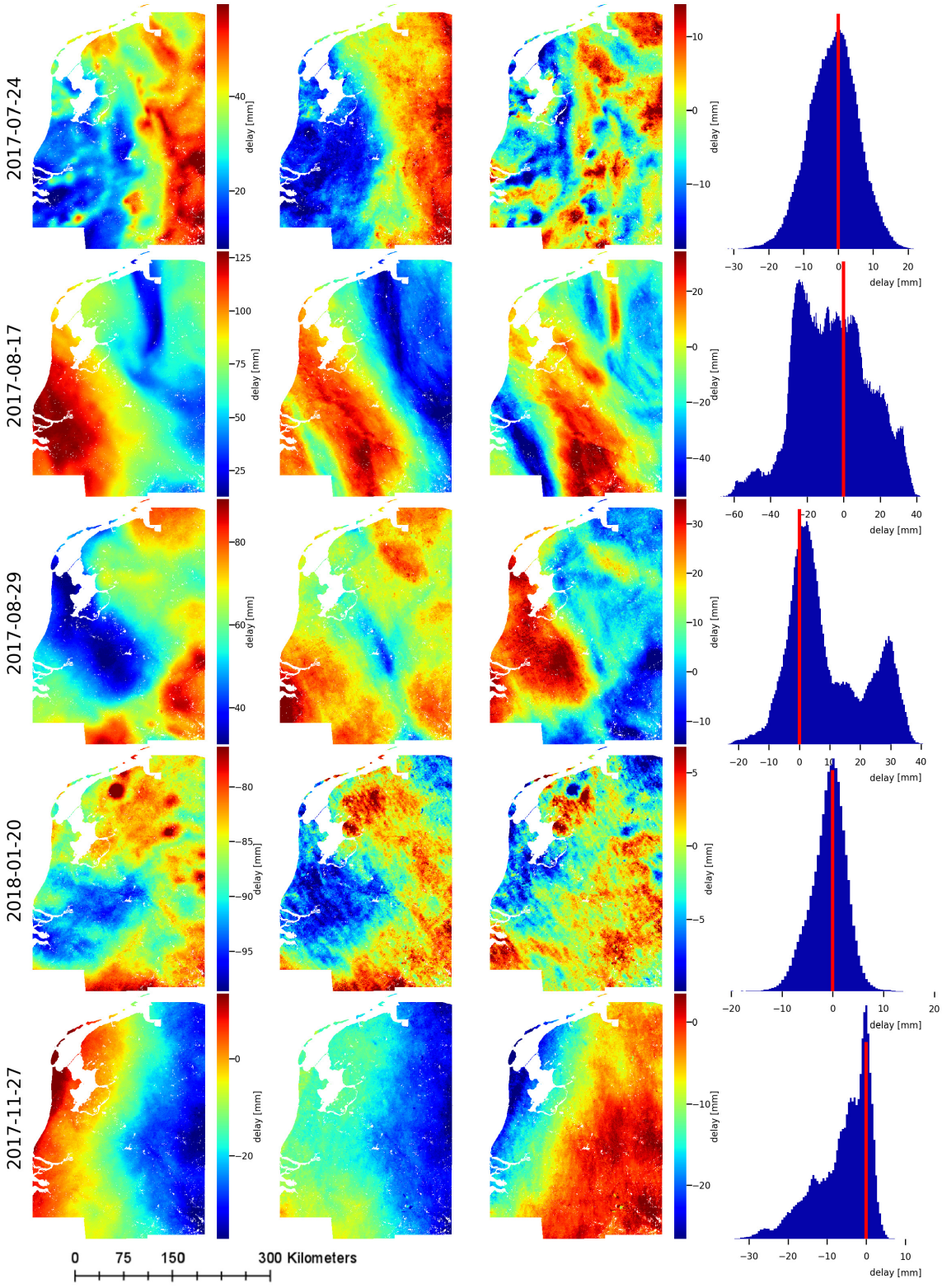

Fig. 6. Comparison between estimated single-epoch atmospheric delays and NWP model derived delays during five satellite overpasses over The Netherlands. Column 1: NWP model delays $\delta^{t_i}_{\text{NWP}}$. Column 2: final estimated single-epoch delays $\hat{\delta}^{t_i}$. Column 3: difference map. Column 4: distribution of the differences. Columns 1 and 2 share the same color bar. These images capture strong convective events (rows 1 and 4) and frontal movements (row 2), but also large regions with different delays (rows 3 and 5).

where $\sigma^2_{\text{NWP}}(t_i)$ is the standard deviation for the same (virtual) daisy-chain interferometric combinations and P is the number of pixels in the image. Fig. 10 shows that these absolute residuals, in orange, are about ten times greater than the absolute residuals with the interferograms, i.e., 10 mm (orange dots), and 1 mm (blue crosses). These values also

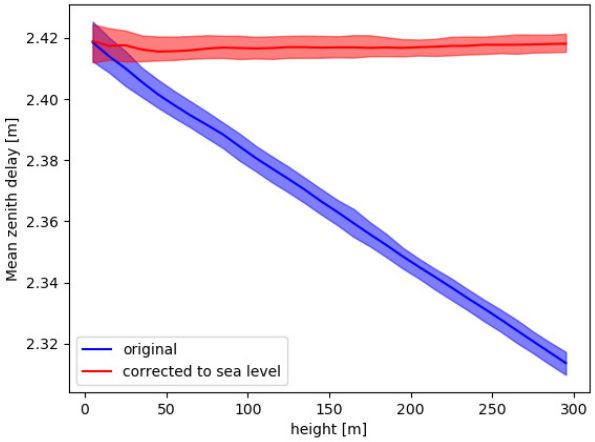

Fig. 7. Single-epoch delay $\hat{\delta}_{h,p}^{t_i}$ as a function of elevation, in blue. By applying a linear scaling factor of 1 mm/m, we artificially "correct" for topography, $\hat{\delta}_{\text{zenith},h,p}^{t_i}$, in red. The shaded area is the one standard deviation interval of these height bins.

give an indication for the maximum deformation within one six-day interval, which will show up in the residuals of the interferograms. As long as the mean residuals between the NWP and InSAR data are an order of magnitude larger than the deformation within one epoch, the deformation values will be of marginal influence on the final estimate NWP estimate, allowing for a mean deformation of some mm in our case. Part of the difference between the NWP model and the estimated delay is caused by resolution differences between the NWP and InSAR data, which can also be seen from the results shown in Fig 6, where the patterns in the first column are smoother than in the second column as a result of a lower input resolution. Therefore, a downsampled version of the 500-m estimated delay should be used for direct assimilation in the NWP model, although the high-resolution InSAR data can still be used for parameterization of small-scale processes in the model. Delay differences also have a strong spatial correlation and increase over larger distances, so the effect of local variations on a smaller scale than the NWP model resolution stays within a few millimeters.

D. Mitigation of Nonatmospheric Delays Using NWP Model Data

The use of NWP delay measurements for every time step prevents our solution to drift over time due to nonatmospheric effects, such as deformation and decorrelation. For deformation, this is caused by the "leaking" of deformation signal into the delay estimation. Decorrelation, on the other hand, initiates a random walk process of the solution over time due to higher uncertainties, as shown in Fig. 11. Using the NWP-derived delays as a constraint for the final solution mitigates these drifts. Note that methods that apply a free network, such as SBAS [21] or phase linking [22], would cause the solution to drift for our application. Fig. 11 shows this drift as a function of time from the last NWP model reference, both for cells with a high coherence ($\gamma > 0.5$, in red) as well as for cells with a low coherence ($\gamma < 0.2$, in blue). Clearly, a lower coherence induces a higher likelihood of drift. The

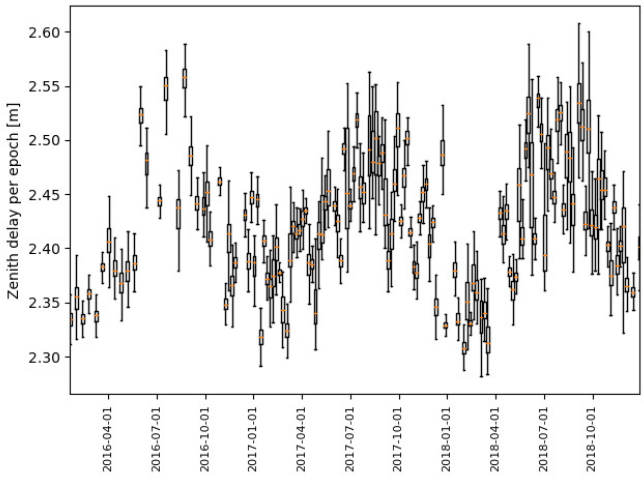

Fig. 8. Estimated topography-adjusted single-epoch zenith delay values $\hat{\delta}_{\text{zenith},h,p}^{t_i}$ as a function of time. The delays are given as box plots for every individual epoch. This shows a seasonal trend in delays, which is due to temperature and moisture changes, as the variation in total air pressure can only explain a minor change in total delay.

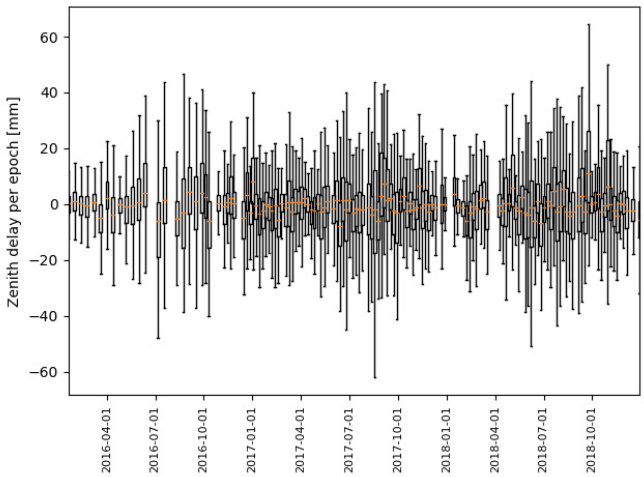

Fig. 9. Spread of difference between NWP model delays $\delta_{\text{NWP,zenith},p}^{t_i}$ and estimated single-epoch delays $\hat{\delta}_{\text{zenith},p}^{t_i}$ per acquisition. The delay differences are given as box plots for every individual epoch. This shows that the differences in the summer tends to be larger than in winter.

bandwidths cover a 95% interval of the datasets, and the solid lines show the average drift. The used network for SBAS and our method uses the same interferometric combinations based on a maximum temporal baseline of 60 days. Although the use of NWP model data can filter out InSAR errors due to deformation and decorrelation, the final delay estimate becomes vulnerable to long-term or systematic errors in the NWP model. To ensure the reliability of NWP models for interseasonal or climatological changes, it is therefore not possible to rely on InSAR measurements only.

E. Estimation Accuracy of Common Mode

Without an external data source, it is not possible to find the common mode $\delta_{\text{cm},p}$ [see (1)]. In our case, this is done by using the NWP model data, which gives a reference value for all individual pixels in the image, but there are also alternatives

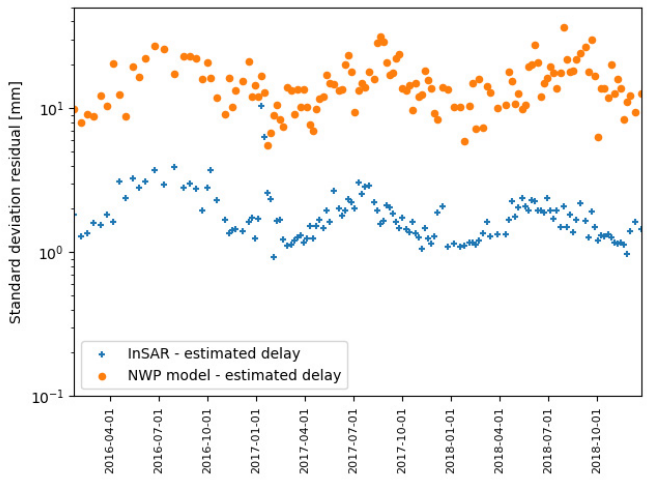

Fig. 10. Standard deviation of the residuals of: 1) daisy-chain interferograms and the difference of the single-epoch solutions (blue) and 2) difference NWP realizations and the difference of the single-epoch solutions (orange). This shows that almost all interferometric atmospheric information is sustained in the final atmospheric delay estimation (blue). The difference between the NWP model and the InSAR data (orange) is about ten times larger than the difference of the single-epoch estimates with the InSAR data.

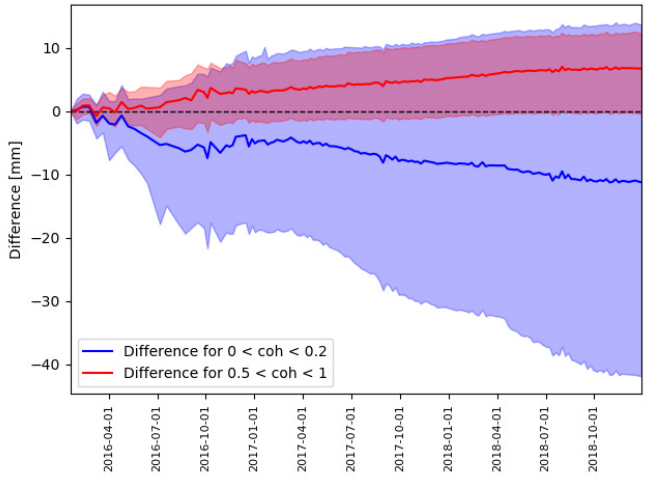

Fig. 11. Solution drift if a nonconstrained model such as SBAS would be used to derive atmospheric delays. To compare our single-epoch delay estimation with an SBAS solution, we take the first date of the time series as a reference and subtract our single-epoch solution from the SBAS solution for the other dates. The red line shows the average drift for high-coherent points, which may also be a consequence of a deformation signal in the SBAS solution. The blue line gives the average drift of the low-coherent points. The shaded area gives the 95% interval for both datasets.

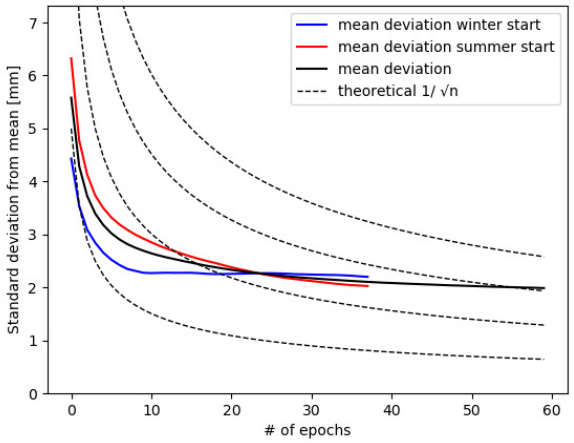

Fig. 12. Comparison of expected standard deviation of the mean atmospheric delay using the final values mapped to the zenith. The dashed lines show the behavior if the data are Gaussian and the other lines show the actual standard deviation of the mean for all values mapped to the zenith, $\hat{\delta}^{t_i}_{\text{zenith},p}$. The dotted lines give expected standard deviation if the dataset would be Gaussian for an average error of 5, 10, 15, and 20 mm. This shows that the mean deviation decreases much slower for a larger number of epochs than one would expect with a Gaussian process and indicates that InSAR atmospheric delays are likely non-Gaussian.

where only partial coverage, e.g. MERIS, or a number of reference points, e.g. GNSS, are used. Some methods also try to replace this common mode by introducing a time series average, assuming that the mean delays of all pixels will become the same after enough averaging [19]. An important assumption for the use of these methods is that the available data on the common mode can be interpolated in space and possible errors will average out over time. However, averaging in space will cause problems in the case of significant topography or climatological differences. Fig. 7 shows that there is a strong dependence on topography, which can only partly be incorporated in the interpolation process. Moreover, the variation in atmospheric delays between two reference points in space can be highly irregular and does not behave Gaussian. Fig. 12 shows that the averaging of InSAR APS measurements in time averages out slower than the assumed $1/(n)^{1/2}$ in case of a Gaussian process, where n is the total number of images. Therefore, one should be cautious to use external data with a low coverage in time and space to find the common mode $\delta_{\text{cm},p}$. In our method, the common mode is estimated using NWP data. Although the common-mode estimation in this method does not need spatial averaging and is therefore much less affected by spatial variability, it does depend on the time series length. In this case, we are not just averaging the InSAR measurements over time, but the InSAR minus the NWP measurements to find the common mode. This will eliminate most topography and climatological errors but still depends on averaging out the error between NWP and InSAR data. Based on the residuals between the estimated delays and NWP data, these values will be about 2 mm (see Fig. 12).

F. Sensitivity of Delay Estimate to Chosen Maximum Temporal Baseline

The selected maximum temporal baseline is a tradeoff between an increasing number of interferograms used, and therefore better use of interferometric information, at the expense of potentially higher temporal decorrelation and larger surface deformation, degrading the estimated delay and accuracies. InSAR accuracy due to temporal decorrelation can be estimated based on coherence, but the time scale of this decorrelation process varies from pixel to pixel. However, deformation signals are not related to coherence and increase over time for the whole study area. Also, low coherence values are biased and have low accuracy and the associated

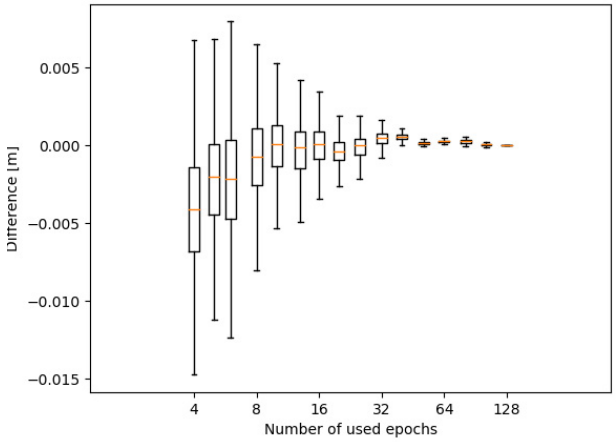

Fig. 13. Difference in result for final atmospheric delay estimation for a different number of acquisitions (epochs), relative to the reference case with 128 images. The box plots express the expected error in the estimated atmospheric delay $\hat{\delta}^{t_i}$ due to the use of less acquisitions. Solutions show an average error of less than 1 mm for 40 epochs when we use a 500-m InSAR grid and temporal baseline of 60 days.

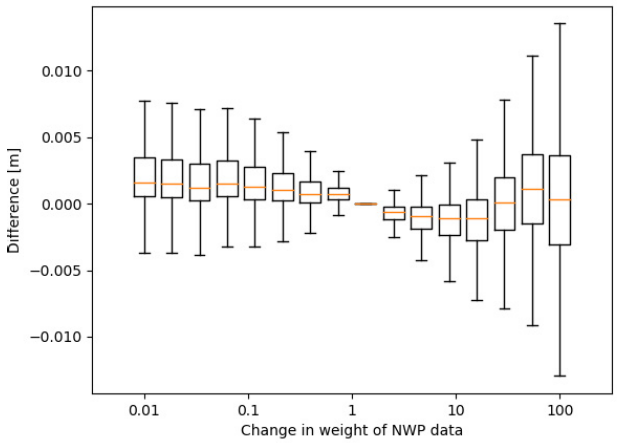

Fig. 14. Effect of the weight of the influence of the NWP-derived delay on the solution. Decreasing or increasing the weight of the NWP leads to differences with the reference solution, indicated with unit weight. This shows that the current solution is relatively stable but does change using different weights. With very low weights, the model will only act as a reference to derive the common mode, $\delta_{\mathrm{cm},p}$, while with higher weights, the model will start smoothing out the InSAR variance in the final estimate.

interferograms should be excluded from the estimation process when possible. Based on these considerations and estimated coherence, a temporal baseline of 60 days is used in this study.

G. Sensitivity of Delay Estimate to Time Series Length

An important factor to consider when applying this method is the minimum number of acquisitions to produce a reliable result. We produced constrained least-squares solutions for different numbers of acquisitions and compared the corresponding atmospheric delay estimates $\hat{\delta}^{t_i}$ with the longest time series solution of 128 acquisitions (see Fig. 13). The results indicate that the uncertainties become on average less than 1 mm for time series length of 40 acquisitions or more when we use a 500 InSAR grid. For Sentinel-1, this corresponds to eight-month consecutive acquisitions. Fig. 13 also shows the expected errors if we only use one interferogram, i.e., two epochs, to find a solution.

H. Sensitivity of Delay Estimate to NWP Model Accuracy

As described in Section II-F, the spatially smoothed difference between the InSAR and predicted NWP data is used as a proxy for the NWP model quality, expressed in Q_δ [see (22)]. The inverse of Q_δ acts as a weighting factor for the influence of the NWP model on the final solution. Because the NWP model weights are an order of magnitude smaller than the InSAR weights, this solution stays relatively close to the InSAR results. In Fig. 14, we demonstrate the impact of an increased (or decreased) weight of the NWP on the solution. This shows that both increasing and decreasing the weight lead to differences with the reference solution, here indicated with unit weight. Decreasing the weight leads to differences of a couple of millimeters relative to the reference solution, up to the limit where changes in NWP model weight have no practical influence on the solution anymore, as the box plots remain nearly identical. In that case, the NWP only functions to find the common mode $\delta_{\mathrm{cm},p}$ (see Section I). Increasing the weights leads to constantly increasing differences, up to the level where the InSAR data become irrelevant and the final solution is the NWP model itself.

I. Possible Improvement of InSAR and NWP Model Accuracy Estimates

A reliable error estimation for InSAR and NWP model data is an important component in our methodology, especially as the accuracy of NWP model data was not available beforehand. For InSAR data, we now used the coherence values, but noise signals could also be estimated using a local variance factor, which uses arcs with neighboring pixels [26]. This allows us to remove most of the spatially correlated atmospheric signals to estimate InSAR noise and local deformation. However, this method should include additional averaging in time or space, which makes the error estimate less specific. To improve the coherence estimate, a selection of areas with homogeneous scattering characteristics could be applied [43], [44]. Assuming linear deformation, we could also decrease the estimated accuracy of the InSAR signal with larger temporal baselines. Finally, the derived InSAR accuracies can be used to improve the estimated variance of the NWP model data given in (20), but this becomes only relevant with decreasing InSAR accuracies.

IV. Conclusion

Based on a constrained least-squares estimation using InSAR and NWP model realizations, we demonstrate a robust and accurate estimation method for absolute single-epoch atmospheric delays, with a deviation from the original InSAR data of only 1-mm delay. This deviation is consistent over almost all epochs and shows a seasonal trend (see Section III-C). As the NWP model accuracy was unknown, we developed a new method to estimate NWP model accuracy (see Section II-F), which is used in the constrained least squares to give an absolute reference to the InSAR estimates.

This method enables the weather modeling community to obtain absolute atmospheric delays with a high resolution of 500 m and unprecedented accuracy of about 1-mm delay, which are ready for assimilation in operational weather models. Observed mean differences of 10 mm between the estimated delays and NWP models suggest a large potential for NWP model improvement. The method does not require external data sources such as GNSS or MERIS, is able to overcome potential observation gaps due to surface decorrelation, and minimizes the effect of long-term deformation patterns.

REFERENCES

[1] P. Bauer, A. Thorpe, and G. Brunet, "The quiet revolution of numerical weather prediction," *Nature*, vol. 525, no. 7567, pp. 47–55, Sep. 2015, doi: 10.1038/nature14956.

[2] Z. Pu and E. Kalnay, "Numerical weather prediction basics: Models, numerical methods, and data assimilation," in *Proc. Handbook Hydrometeorological Ensemble Forecasting*. Berlin, Germany: Springer, 2018, pp. 1–31.

[3] R. F. Hanssen, T. M. Weckwerth, H. A. Zebker, and R. Klees, "High-resolution water vapor mapping from interferometric radar measurements," *Science*, vol. 283, no. 5406, pp. 1297–1299, 1999.

[4] P. M. A. Miranda, P. Mateus, G. Nico, J. Catalão, R. Tomé, and M. Nogueira, "InSAR meteorology: High-resolution geodetic data can increase atmospheric predictability," *Geophys. Res. Lett.*, vol. 46, no. 5, pp. 2949–2955, Feb. 2019, doi: 10.1029/ 2018GL081336.

[5] S. Liu and R. F. Hanssen, "Feasibility of retrieving spatial variations of atmospheric phase screen at epochs of SAR acquisitions from SAR interferometry," in *Proc. Fringe Workshop*, 2009, p. 5.

[6] P. Mateus, G. Nico, and J. Catalão, "Can spaceborne SAR interferometry be used to study the temporal evolution of PWV?" *Atmos. Res.*, vol. 119, pp. 70–80, Jan. 2013. [Online]. Available: https://www.sciencedirect.com/science/article/pii/S0169809511003292

[7] E. Pichelli *et al.*, "InSAR water vapor data assimilation into mesoscale model MM5: Technique and pilot study," *IEEE J. Sel. Topics Appl. Earth Observ. Remote Sens.*, vol. 8, no. 8, pp. 3859–3875, Aug. 2015. [Online]. Available: http://ieeexplore.ieee.org/lpdocs/epic03/wrapper.htm?arnumber=6922479

[8] M. Berger, J. Moreno, J. A. Johannessen, P. F. Levelt, and R. F. Hanssen, "ESA's sentinel missions in support of Earth system science," *Remote Sens. Environ.*, vol. 120, pp. 84–90, May 2012.

[9] R. F. Hanssen, A. J. Feijt, and R. Klees, "Comparison of precipitable water vapor observations by spaceborne radar interferometry and meteosat 6.7-μm radiometry," *J. Atmos. Ocean. Technol.*, vol. 18, no. 5, pp. 756–764, May 2001. [Online]. Available: http://doris.tudelft.nl/Literature/hanssen01b.pdf

[10] C. Liang, P. Agram, M. Simons, and E. J. Fielding, "Ionospheric correction of InSAR time series analysis of C-band sentinel-1 tops data," *IEEE Trans. Geosci. Remote Sens.*, vol. 57, no. 9, pp. 6755–6773, Sep. 2019.

[11] P. Mateus, P. M. A. Miranda, G. Nico, J. Catalão, P. Pinto, and R. Tomé, "Assimilating InSAR maps of water vapor to improve heavy rainfall forecasts: A case study with two successive storms," *J. Geophys. Res., Atmos.*, vol. 123, pp. 3341–3355, Apr. 2018, doi: 10.1002/2017JD027472.

[12] P. Mateus, R. Tomé, G. Nico, and J. Catalão, "Three-dimensional variational assimilation of InSAR PWV using the WRFDA model," *IEEE Trans. Geosci. Remote Sens.*, vol. 54, no. 12, pp. 7323–7330, Dec. 2016. [Online]. Available: http://ieeexplore.ieee.org/document/7557071/

[13] P. Courtier *et al.*, "The ECMWF implementation of three-dimensional variational assimilation (3D-var). I: Formulation," *Quart. J. Roy. Meteorol. Soc.*, vol. 124, no. 550, pp. 1783–1807, Jul. 1998, doi: 10.1002/qj.49712455002.

[14] F. Rabier, H. Järvinen, E. Klinker, J.-F. Mahfouf, and A. Simmons, "The ECMWF operational implementation of four-dimensional variational assimilation. I: Experimental results with simplified physics," *Quart. J. Roy. Meteorol. Soc.*, vol. 126, no. 564, pp. 1143–1170, Jul. 2007, doi: 10.1002/qj.49712656415.

[15] S. de Haan, "Assimilation of GNSS ZTD and radar radial velocity for the benefit of very-short-range regional weather forecasts," *Quart. J. Roy. Meteorol. Soc.*, vol. 139, no. 677, pp. 2097–2107, Oct. 2013.

[16] M. Bevis *et al.*, "GPS meteorology: Mapping zenith wet delays onto precipitable water," *J. Appl. Meteorol.*, vol. 33, no. 3, pp. 379–386, Mar. 1994.

[17] P. Mateus, J. Catalão, and G. Nico, "Sentinel-1 interferometric SAR mapping of precipitable water vapor over a country-spanning area," *IEEE Trans. Geosci. Remote Sens.*, vol. 55, no. 5, pp. 2993–2999, May 2017. [Online]. Available: http://ieeexplore.ieee.org/document/7855708/

[18] R. F. Hanssen, "Radar Interferometry: Data interpretation and error analysis," Ph.D. dissertation, Dept. Geosci. Remote Sens., Delft Univ. Technol., Delft, The Netherlands, 2001.

[19] S. Liu, "Satellite radar interferometry: Estimation of atmospheric delay," Ph.D. dissertation, Dept. Geosci. Remote Sens., Delft Univ. Technol., Delft, The Netherlands, 2013.

[20] F. V. Leijen and R. Hanssen, "Interferometric radar meteorology: Resolving the acquistion ambiguity," in *Proc. CEOS SAR Workshop*, 2004, pp. 27–28.

[21] P. Berardino, G. Fornaro, R. Lanari, and E. Sansosti, "A new algorithm for surface deformation monitoring based on small baseline differential SAR interferograms," *IEEE Trans. Geosci. Remote Sens.*, vol. 40, no. 11, pp. 2375–2383, Nov. 2002. [Online]. Available: http://ieeexplore.ieee.org/document/1166596/

[22] A. M. Guarnieri and S. Tebaldini, "On the exploitation of target statistics for SAR interferometry applications," *IEEE Trans. Geosci. Remote Sens.*, vol. 46, no. 11, pp. 3436–3443, Nov. 2008. [Online]. Available: http://ieeexplore.ieee.org/document/4685949/

[23] A. Hooper, P. Segall, and H. Zebker, "Persistent scatterer interferometric synthetic aperture radar for crustal deformation analysis, with application to Volcán alcedo, Galápagos," *J. Geophys. Res.*, vol. 112, no. B7, pp. 1–21, 2007.

[24] A. Ferretti, C. Prati, and F. Rocca, "Permanent scatterers in SAR interferometry," *IEEE Trans. Geosci. Remote Sens.*, vol. 39, no. 1, pp. 8–20, Jan. 2001.

[25] A. Ferretti, C. Prati, and F. Rocca, "Process for radar measurements of the movement of city areas and landsliding zones," U.S. Patent 6 583 751 B1, Nov. 30, 2011.

[26] F. V. Leijen, "Persistent Scatterer Interferometry based on geodetic estimation theory," Ph.D. dissertation, Dept. Geosci. Remote Sens., Delft Univ. Technol., Delft, The Netherlands, 2014.

[27] P. Benevides, G. Nico, J. Catalao, and P. M. A. Miranda, "Bridging InSAR and GPS tomography: A new differential geometrical constraint," *IEEE Trans. Geosci. Remote Sens.*, vol. 54, no. 2, pp. 697–702, Feb. 2016. [Online]. Available: http://ieeexplore.ieee.org/document/7293637/

[28] F. Alshawaf, S. Hinz, M. Mayer, and F. J. Meyer, "Constructing accurate maps of atmospheric water vapor by combining interferometric synthetic aperture radar and GNSS observations," *J. Geophys. Res., Atmos.*, vol. 120, no. 4, pp. 1391–1403, Feb. 2015, doi: 10.1002/2014JD022419.

[29] F. Meyer, R. Bamler, R. Leinweber, and J. Fischer, "A comparative analysis of tropospheric water vapor measurements from MERIS and SAR," in *Proc. IEEE Int. Geosci. Remote Sens. Symp. (IGARSS)*, 2008, pp. IV228–IV231. [Online]. Available: http://ieeexplore.ieee.org/document/4779699/

[30] B. Puysségur, R. Michel, and J.-P. Avouac, "Tropospheric phase delay in interferometric synthetic aperture radar estimated from meteorological model and multispectral imagery," *J. Geophys. Res.*, vol. 112, no. B5419, pp. 1–12, 2007, doi: 10.1029/2006JB004352.

[31] F. J. Meyer, "Performance requirements for ionospheric correction of low-frequency SAR data," *IEEE Trans. Geosci. Remote Sens.*, vol. 49, no. 10, pp. 3694–3702, Oct. 2011. [Online]. Available: http://ieeexplore.ieee.org/document/5783915/

[32] P. J. G. Teunissen, D. G. Simons, and C. C. J. M. Tiberius, *Probability and Observation Theory*. Delft, The Netherlands: TU Delft, 2006. [Online]. Available: https://books.google.nl/books?id=ba-SnQEACAAJ

[33] S. De haan, "Meteorological applications of a surface network of global positioning system receivers," Ph.D. dissertation, Wagening Univ. Res., Wageningen, The Netherlands, 2008.

[34] H. Vedel, K. S. Mogensen, and X.-Y. Huang, "Calculation of zenith delays from meteorological data comparison of NWP model, radiosonde and GPS delays," *Phys. Chem. Earth, A, Solid Earth Geodesy*, vol. 26, nos. 6–8, pp. 497–502, Jan. 2001.

[35] C. W. Chen and H. A. Zebker, "Phase unwrapping for large SAR interferograms: Statistical segmentation and generalized network models," *IEEE Trans. Geosci. Remote Sens.*, vol. 40, no. 8, pp. 1709–1719, Aug. 2002. [Online]. Available: http://ieeexplore.ieee.org/document/1036000/

[36] R. F. Hanssen, A. J. Feijt, and R. Klees, "Comparison of precipitable water vapor observations by spaceborne radar interferometry and meteosat 6.7-μm radiometry," *J. Atmos. Ocean. Technol.*, vol. 18, no. 5, pp. 756–764, May 2001.
[37] G. D. Thayer, "An improved equation for the radio refractive index of air," *Radio Sci.*, vol. 9, no. 10, pp. 803–807, 1974.
[38] J. M. Rüeger, "Refractive index formulae for radio waves," in *Proc. FIG 22nd Int. Congr.*, Washington, DC, USA, vol. 113, 2002, pp. 1–13.
[39] R. Dach *et al.*, "Code final product series for the IGS," Astronomical Inst., Univ. Bern, Bern, Switzerland, Tech. Rep. 75876, 2016.
[40] R. Touzi, A. Lopes, J. Bruniquel, and P. W. Vachon, "Coherence estimation for SAR imagery," *IEEE Trans. Geosci. Remote Sens.*, vol. 37, no. 1, pp. 135–149, Jan. 1999. [Online]. Available: http://ieeexplore.ieee.org/document/739146/
[41] L. Bengtsson *et al.*, "The HARMONIE-AROME model configuration in the ALADIN-HIRLAM NWP system," *Monthly Weather Rev.*, vol. 145, no. 5, pp. 1919–1935, 2017.
[42] T. Palmer, "The ECMWF ensemble prediction system: Looking back (more than) 25 years and projecting forward 25 years," *Quart. J. Roy. Meteorol. Soc.*, vol. 145, no. S1, pp. 12–24, Sep. 2019.
[43] S. S. Esfahany, "Exploitation of distributed scatterers in synthetic aperture radar interferometry," Ph.D. dissertation, Dept. Geosci. Remote Sens., Delft Univ. Technol., Delft, The Netherlands, 2017. [Online]. Available: https://doi.org/10.4233/ uuid:22d46f1e-9061-46b0-9726-760c41404b6f
[44] A. Ferretti, A. Fumagalli, F. Novali, C. Prati, F. Rocca, and A. Rucci, "A new algorithm for processing interferometric data-stacks: SqueeSAR," *IEEE Trans. Geosci. Remote Sens.*, vol. 49, no. 9, pp. 3460–3470, Sep. 2011. [Online]. Available: http://ieeexplore.ieee.org/document/5765671/

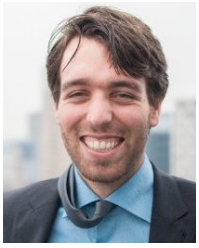

Gert Mulder was born in 1988. He received the B.Sc. degree in civil engineering and the M.Sc. degree in hydrology and water management from the Delft University of Technology (DUT), Delft, The Netherlands, in 2010 and 2014, respectively.

Since 2014, he worked on the water accounting concept based on remote sensing products at IHE, Delft, before he started his Ph.D. research in 2015 on the application of InSAR atmospheric signals in weather models as a joined study between DUT and the Royal Netherlands Meteorological Institute (KNMI), De Bilt, The Netherlands. From 2019 to 2021, he worked as a Researcher for the Harmony mission, the current Earth Explorer 10 candidate. His main research interest is the study of hydrological processes based on remote sensing products for a wide range of applications, including atmospheric processes, land surface models, and rainfall-runoff models.

Freek J. van Leijen (Member, IEEE) received the master's degree in geodetic engineering from the Delft University of Technology, Delft, The Netherlands, in 2002, and the Ph.D. degree from the Delft University of Technology in 2014, working on InSAR research. His master's thesis concerned the stochastic modeling of the tropospheric variability using GPS and InSAR observations.

He has developed a range of software algorithms for persistent scatterer interferometry. After working for five years at SkyGeo, Delft, a commercial company delivering radar remote sensing services, he returned to the Delft University of Technology in 2013 to continue his research in the field of satellite radar interferometry.

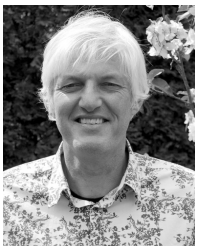

Jan Barkmeijer studied mathematics at Rijksuniversiteit Groningen (RUG), Groningen, The Netherlands. He received the Ph.D. degree from RUG in 1988, with a focus on chaos theory.

From 1995 to 2002, he was employed at the European Centre for Medium-Range Weather Forecasts, Reading, U.K., where he was closely involved in the development of the ECMWF ensemble. He is currently working as a Senior Scientist with the Weather and Climate Modeling Department, Royal Netherlands Meteorological Institute (KNMI), De Bilt, The Netherlands, with particular interest in predictability research and data assimilation.

Siebren de Haan received the Ph.D. degree in mathematics and meteorology from the University of Wageningen, Wageningen, The Netherlands, in May 2008.

He is currently a Researcher with the Weather Research Department, Royal Netherlands Meteorological Institute (KNMI), De Bilt, The Netherlands. He worked for two years on the assimilation of satellite-derived sea surface temperatures for use in numerical weather prediction models and on an ice detection algorithm using backscatter data from the ERS satellites within the EUMETSAT Ocean and Sea Ice Satellite Application Facility. He is currently a responsible member of the EUMETNET GPS Water Vapour Programme (E-GVAP II), actively involved in the EUMETNET NOWCAST program, a member of the WMO CIMO Expert Team on New Technologies and Test Beds, and a member of the MTG-IRS Science Team. Very recent activities are related to novel wind and temperature observations from commercial aircraft exploiting Mode-S Enhanced Surveillance information.

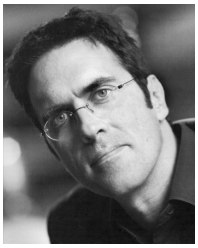

Ramon F. Hanssen (Senior Member, IEEE) received the M.Sc. degree in geodetic engineering and the Ph.D. degree *(cum laude)* from the Delft University of Technology, Delft, The Netherlands, in 1993 and 2001, respectively.

He was with the International Institute for Aerospace Survey and Earth Science (ITC), University of Stuttgart, Stuttgart, Germany; the German Aerospace Center (DLR), Weßling, Germany; Stanford University, Stanford, CA, USA, as a Fulbright Fellow; and the Scripps Institution of Oceanography, University of California at San Diego, La Jolla, CA, where he was involved in microwave remote sensing, radar interferometry, signal processing, and geophysical application development. Since 2008, he has been an Antoni van Leeuwenhoek Professor in Earth observation with the Delft University of Technology, where he has been leading the research group on mathematical geodesy and positioning since 2009. He has authored a textbook on radar interferometry.